Cellular interface morphologies in directional solidification. III. The effects of heat transfer and solid diffusivity

Lyle H. Ungar,* Mark J. Bennett, and Robert A. Brown
Department of Chemical Engineering and Materials Processing Center, Massachusetts Institute of Technology, Cambridge, Massachusetts 02139
(Received 1 November 1984)

The shape and stability of two-dimensional finite-amplitude cellular interfaces arising during directional solidification are compared for several solidification models that account differently for latent heat released at the interface, unequal thermal conductivities of melt and solid, and solute diffusivity in the solid. Finite-element analysis and computer-implemented perturbation methods are used to analyze the families of steadily growing cellular forms that evolve from the planar state. In all models a secondary bifurcation between different families of finite-amplitude cells exists that halves the spatial wavelength of the stable interface. The quantitative location of this transition is very dependent on the details of the model. Large amounts of solute diffusion in the solid retard the growth of large-amplitude cells.

I. INTRODUCTION

The evolution of steadily growing cellular melt-solid interfaces from an initially unstable planar front has received much attention because of the relationship of the nonlinear interactions inherent in these transformations to the processes involved in the formation of more complex solidification patterns. The physics describing the onset of cellular growth is well developed in the linear-stability analysis of Mullins and Sekerka.[1] Using either the growth velocity V of the interface or the temperature gradient $\tilde{G}$ as a control parameter, periodic undulations develop along a flat interface at particular values of V or $\tilde{G}$ for specific spatial wavelengths. The wavelength corresponding to the lowest growth rate or highest-temperature gradient for instability is the most dangerous. In the analysis that follows we study the evolution of steadily growing cellular interfaces that originate with fixed wavelength from the small-amplitude states predicted by linear-stability analysis. In doing so we concentrate on predicting the evolution from the planar interface to deep cellular interfaces, while relying on the hypothesis that such a transition can be predicted without accounting for continuous changes in the spatial frequency of individual cells. The problem of predicting the mean spatial wavelength of a front of growing cells has been investigated previously by examining the stability of fixed-wavelength cells of small amplitude to shape perturbations with longer wavelength,[2,3] but no deterministic theory for predicting changes in wavelength has been derived.

Several research groups[4–7] have computed, either asymptotically or numerically, the steadily growing cells which evolve at specific spatial wavelengths. In a recent paper (Ref. 6, henceforth referred to as UB) we have used ideas from bifurcation theory to describe the formation of deep two-dimensional cellular interfaces for a simplified solidification system where the thermal properties of both phases are taken to be equal, latent-heat release at the interface and convective heat transfer are neglected, and the solute diffusivity in the solid is ignored. Families of interfaces with shapes represented by a Cartesian Monge' projection onto the planar front were computed as the temperature gradient was decreased. One of the important findings of this research was the existence of a secondary bifurcation point between the shape family evolving from the values of $\tilde{G}$ for neutral stability to small perturbations with the critical wavelength and shapes with wavelength of half the critical value. Because of this bifurcation, the stable family of cells evolved to lower values of $\tilde{G}$ with wavelength $\bar{\lambda}_c/2$ for all interface shapes that were representable by the Monge' projection. For the calculations presented in UB, the secondary bifurcation occurred at a temperature gradient so close to the critical value of linear theory that only cells with half of the critical wavelength are expected to be observed.

One of the aims of the present paper is to show that this nonlinear transition is generic to a wide range of solidification models, thus better establishing its importance in the modeling of large-amplitude two-dimensional cells. To do this we consider a general thermal-solutal solidification model (TSM) which accounts for the coupling of heat and solute transport in the melt and solid regions and for the release of latent heat at the melt-solid interface. We assume that the interface is in local equilibrium with respect to solute and temperature and so still neglect any effects of growth-rate kinetics on the interface morphology.[8] The simplified solidification models used in other analyses are summarized in Table I according to the assumptions made in each concerning the release of latent heat at the interface, the thermal conductivities of the melt and solid, convective heat transport in the bulk phases, and the diffusivities of solute in both phases. The model used in the original analysis of Mullins and Sekerka corresponds to our one-sided TSM where solute dif-

TABLE I. Summary of models used for studying the formation of cellular melt-solid interfaces during directional solidification.

Model	Latent heat	Thermal conductivities	Convective heat transport	Solid diffusion	Reference
Thermal-solutal (TSM)	yes	not equal	yes	yes	a
One-sided TSM	yes	not equal	yes	no	b
Equal conductivity	yes	equal	yes	no	c
Solutal model (SM)	no	equal	no	yes	a
Symmetric SM	no	equal	no	yes ($\mathscr{D}_L=\mathscr{D}_S$)	d
One-sided SM	no	equal	no	no	e

[a]Reference 11.
[b]Reference 1.
[c]Reference 7.
[d]Reference 5.
[e]Reference 6.

fusivity in the solid has been neglected. The one-sided solutal model (SM) was used in the analysis presented in UB.

The mathematical representations of the models listed in Table I are presented in Sec. II along with the results for the general linear-stability analysis. When solute diffusivity in the solid is neglected the neutral stability limits can be superimposed by expressing the critical temperature gradient in terms of an averaged value computed between melt and solid and weighted with the thermal diffusivities of each phase, similar to the expression given in Ref. 1. The formulation of the finite-element technique and the methods for computer-implemented analysis of bifurcation and stability have been detailed in UB and only the slight differences needed to generalize the methodology to the present models are discussed in Sec. II. The results of the calculations for the various models are described in Sec. III.

II. MODELS OF SOLIDIFICATION

We follow the approach developed in UB and view the solidification of a binary melt from a reference frame attached to a planar melt-solid interface moving at the constant growth velocity V. Field variables are described in the Cartesian-coordinate system shown in Fig. 1, where the melt-solid interface is given as a single-valued function, $\tilde{y}=\tilde{h}(\tilde{x})$. The equations governing the full thermal-solutal model are presented in this coordinate system in the dimensionless form obtained by scaling lengths with a characteristic wavelength λ^*, concentration with the value in the melt far from the interface, c_∞, time with, λ^{*2}/D, and temperature with the melting point of pure material along a flat interface, T_m^0.

When the only form of bulk convection in the melt is due to the unidirectional solidification, the equations for heat and solute transport are

$$\nabla^2 c + P\frac{\partial c}{\partial y} = \frac{\partial c}{\partial t} , \tag{2.1}$$

$$\nabla^2\theta + P_t\frac{\partial\theta}{\partial y} = L_e\frac{\partial\theta}{\partial t} \tag{2.2}$$

in the melt, and

$$R_m\nabla^2 c + P\frac{\partial c}{\partial y} = \frac{\partial c}{\partial t} , \tag{2.3}$$

$$R\nabla^2\theta + P_t\frac{\partial\theta}{\partial y} = L_e\frac{\partial\theta}{\partial t} \tag{2.4}$$

in the solid. In these equations, $P=V\lambda^*/D$ is the solutal Peclet number, $P_t\equiv V\lambda^*/\kappa$ is the thermal Peclet number, $L_e=D/\alpha$ is the Lewis number, and $R=\kappa_s/\kappa$ and $R_m\equiv D_s/D$ are the ratios of the solid to the melt conductivities and diffusivities, respectively. Along the melt-solid interface the temperature and solute fields are prescribed to be in local equilibrium as given by the Gibbs-Thomson condition

$$\theta = 1 + mc + 2\Gamma H , \tag{2.5}$$

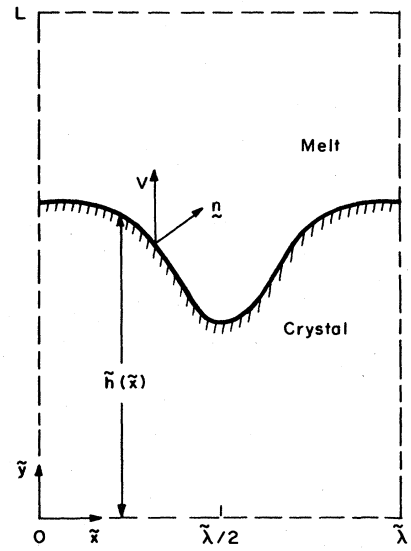

FIG. 1. Schematic of melt and solid regions considered in model for directional solidification. Wavelength of cell is denoted by $\tilde{\lambda}$.

and a liquidus curve of an ideal phase diagram, where $m=\tilde{m}c_\infty/T_m^0$ is the dimensionless slope of the liquidus curve and $\Gamma=\tilde{\Gamma}/\lambda^*$ is the capillary constant. The mean curvature H of the interface is given by the expression

$$2H=\frac{d^2h/dx^2}{[1+(dh/dx)^2]^{3/2}} . \tag{2.6}$$

Conservation of solute and heat across the interface are given as

$$(\mathbf{n}\cdot\nabla c)_m-R_m(\mathbf{n}\cdot\nabla c)_s=(1-k)c\left[P+\frac{\partial h}{\partial t}\right] , \tag{2.7}$$

$$(\mathbf{n}\cdot\nabla\theta)_m-R(\mathbf{n}\cdot\nabla\theta)_s=S_t\left[P_t+L_e\frac{\partial h}{\partial t}\right] , \tag{2.8}$$

where k is the equilibrium partition coefficient for solute between melt and solid, and $S_t=L/\rho c_p T_m^0$ is the Stefan number which scales the contribution of the latent heat L released along the interface to the sensible heat in the melt at the melting point. The subscripts m and s denote that the expressions are evaluated at the interface in the melt and solid phases, respectively.

The solidification model is completed by specifying the temperature gradients far from the interface as being $G=\tilde{G}\lambda^*/T_m^0$ in the melt and $G_s\equiv\tilde{G}_s\lambda^*/T_m^0$ in the solid. The concentration field is taken to be uniform at the dimensionless value of unity far from the interface in the melt for all models and uniform far into the solid where D_s is not zero. The symmetry conditions enforced on the lateral sides of the cell are written as

$$\frac{\partial\theta}{\partial x}=\frac{\partial c}{\partial x}=0, \quad x=0,\lambda . \tag{2.9}$$

We use the temperature gradient in the melt G as the control parameter in our calculations of families of interface shapes.

The models listed in Table I correspond to particular values of the mass-diffusivity ratio R_m, the thermal-conductivity ratio R, the thermal Peclet number P_t, and the Stefan number S_t. The SM's are recovered by setting $S_t=P=0$, $R=1$, and neglecting the convective-heat-transfer terms in the energy equations in melt and solid; the one-sided solutal model is the special case $R_m=0$, while the symmetric model used by Langer[5] corresponds to $R_m=1$. Previous linear-stability analysis and nonlinear calculations including the effects of the thermal field have used $R_m=0$. The nonlinear finite-difference calculations of McFadden and Coriell[7] also assumed that the thermal conductivities between melt and solid were equal, or $R=1$.

The linear-stability analysis of the general thermal-solutal model, Eqs. (2.1)–(2.10), follows the classical work of Mullins and Sekerka[1] and examines the stability of the planar interface to disturbances written in dimensionless form as $h(x,t)=\hat{h}(t)\cos(\omega x)$, where ω is the dimensionless wave number of the perturbation. We report our results in terms of the dimensionless temperature gradient weighted with the thermal diffusivities in each phase,

$$\bar{G}=\frac{\alpha_s G_s+\alpha G}{\alpha_s+\alpha} , \tag{2.10}$$

which is similar to the gradient first defined by Mullins and Sekerka.[1] For a perturbation with a given wave number ω, the values of the temperature gradient for neutral stability are given by the expression

$$\bar{G}=\frac{m(k-1)P}{k}\left[\frac{\omega^*-P}{\omega^*+(k-1)P-\omega_s^* kR_m}\right]-2\pi\Gamma\omega^2 , \tag{2.11}$$

where

$$\omega^*=P/2+[(P/2)^2+(2\pi\omega)^2]^{1/2} ,$$
$$\omega_s^*=P/2R_m-[(P/2R_m)^2+(2\pi\omega)^2]^{1/2} . \tag{2.12}$$

The values of $\bar{G}$ predicted by Eq. (2.11) for set values of ω are the bifurcation points for families of steadily growing cells evolving from the planar state. In the calculations described below we focus on a value of wavelength λ near the most critical value, where instability of the planar state first occurs at the highest possible value of $\bar{G}$.

III. FINITE-ELEMENT ANALYSIS

The finite-element analysis used for calculation of the large-amplitude cellular interfaces, as well as the computer-implemented perturbation analysis used to track families of solutions and to determine their stability with respect to perturbations that preserve the symmetry introduced by Eq. (2.9), closely follows the methods described in UB and in the references therein. We solve the field equations on the finite domain created by replacing the far-field boundary conditions in the melt with

$$\frac{\partial c}{\partial y}=P(c-1), \quad \frac{\partial\theta}{\partial y}=G, \quad y=L_1 , \tag{3.1}$$

where L_1 is taken to be sufficiently large to minimize the amount of diffusion through this artificial boundary. This parameter was taken to be $L_1=3.5\lambda$ in most of the calculations reported here.

The computational domain along the solid is truncated at a distance L_2 from the original location of the planar interface. The temperature field there is set to a specified value

$$\theta(x,-L_2)=\theta_s , \tag{3.2}$$

where θ_s is picked so that the interface remained in the computational domain. Calculations were performed with a varying temperature gradient in the melt, G. The value of the temperature gradient in this artificial boundary is recovered by calculation from the finite-element solution or, equivalently, from the integral overall heat balance

$$G=RG_s-S_tP_t , \tag{3.3}$$

and the value of the conductivity-weighted gradient $\bar{G}$ is then calculated from Eq. (2.10).

When solid diffusion is included ($R_m\neq 0$) we use the boundary condition

$$\frac{\partial c}{\partial y}=0, \quad y=L_2 . \tag{3.4}$$

Equation (3.4) is equivalent to abruptly setting the dif-

fusivity in the solid equal to zero and approximates the decrease in D_s observed in real materials as the temperature decreases from the melting point. The length L_2 is taken to be sufficiently large that this change in D_s does not affect the shape of the interface.

Galerkin-weighted residual equations are formed using the isotherm-Newton method described in Ettouney and Brown[9] and are expressed in the same mapped coordinate system used in UB. The field equations (2.1)—(2.4), the flux balances at the melt-solid interface (2.7) and (2.8), and the boundary conditions (2.9) and (3.1)—(3.3) are all incorporated in these residual equations. A set of one-dimensional Galerkin equations formed from the Gibbs-Thomson condition (2.5) are used to determine the interface shape $h(x)$.

Separate finite-element expansions are written for the temperature and concentration fields in both phases, and for the interface shape. We use the Lagrangian biquadratic basics for each field variable and the one-dimensional quadratic basis set for $h(x)$. Discretizations using eight elements in each coordinate direction, in the melt and solid, lead to approximately 250 unknowns representing each field variable and to 17 unknowns for the interface shape. The entire set of nearly 1000 equations is solved by Newton's method with the elements in the Jacobian matrix computed analytically as discussed in Ref. 9. The computer-implemented perturbation methods then follow directly, as described in UB.

IV. RESULTS

The calculations reported here are extensions of those in Ref. 6 and thus focus on the same set of thermophysical properties appropriate for the Pb-Sb system that is listed in Table II. The wavelengths used were $\lambda=2.0$ for the low growth velocity ($V=16$ μm/sec, $P=0.8$) and $\lambda=0.09092$ for the high growth rate ($V=1600$ μm/sec, $P=80$). The families of cellular interfaces evolving from the first two critical values $G_c^{(i)}$ were computed as a function of R, R_m, and S_t for fixed growth rate. The corresponding value of the temperature gradient in the solid was computed from Eq. (3.3). Results are separated below according to the two values of growth rate used, for calculations neglecting solid diffusivity, $R_m=0$. The effect of this parameter is examined separately.

A. Low growth velocity

The families of cellular interfaces that evolve from the lowest two critical values of temperature gradient for the lowest growth velocity ($P=0.8$, $V=16$ μm/sec) are represented in Fig. 2 by the maximum interface deflection Δ, computed as

$$\Delta=\max_{0\le x\le\lambda}\{h(x)\}-\min_{0\le x\le\lambda}\{h(x)\}\ , \tag{4.1}$$

expressed as a function of the weighted temperature gradient $\overline{G}$. For this growth velocity, $\lambda=2.0$ was approximately 15% above the critical value of the wavelength corresponding to the highest possible value of $\overline{G}$ when

TABLE II. Thermophysical properties and dimensionless groups representative of Pb-Sb.

Property	Symbol	Value
Segregation coefficient	k	0.4
Bulk concentration of Sb (wt. %)	$\tilde{c}_\infty$	0.02
Slope of liquidus (K/wt. %)	$\tilde{m}$	-5
Mass diffusivity in melt	D	2×10^{-5}
Mass diffusivity in solid	D_s	
Thermal conductivity of melt (J/sec cm K)	k	1.47×10^{-2}
Thermal conductivity of solid (J/sec cm K)	k_s	2.75×10^{-2}
Thermal diffusivity of melt (cm^2/sec)	α	0.11
Thermal diffusivity of solid (cm^2/sec)	α_s	0.20
Latent heat of fusion (J/cm^3 K)	L	2.8×10^{2}
Reference melting temperature (K)	T_m^0	600
Capillary length (cm)	$\tilde{\Gamma}$	8.2×10^{-9}
Reference length scale (cm)	λ^*	1×10^{-2}
Growth rates (cm/sec)	V	$1.6\times10^{-3}, 1.6\times10^{-1}$
Dimensionless slope of liquidus	m	-1.67×10^{-4}
Capillary constant	Γ	8.2×10^{-7}
Mass Peclet numbers	P	0.8, 80
Thermal Peclet numbers	P_t	1.48×10^{-4}, 1.48×10^{-2}
Thermal-conductivity ratio	R	1.87
Mass-diffusivity ratio	R_m	
Stefan number	S_t	0.29

$R_m=0$. All three sets of calculations shown in Fig. 2 have the same critical values predicted from linear theory, as discussed in Sec. II.

The results for $R=1$ and $S_t=0$ are the calculations for the one-sided SM discussed at length in UB and show the secondary bifurcation between the interfaces with the original wavelength and the shapes with wavelength $\lambda/2$. As discussed in UB, this value of $\overline{G}=\overline{G}_s^{(2)}$ was a bifurcation point between interfaces with wavelength $\lambda/2$ and the shape shown in the inset of Fig. 2 and two types of cells with wavelength λ, but differing in whether the undulation has up (the 1U family) or down (the 1D family) at $x=0$.

Introducing the amount of latent heat $S_t=0.29$ appropriate for the Pb-Sb system resulted in the calculations shown by the dashed curves in Fig. 2. Here the primary family of cellular shapes with wavelength λ evolved su-

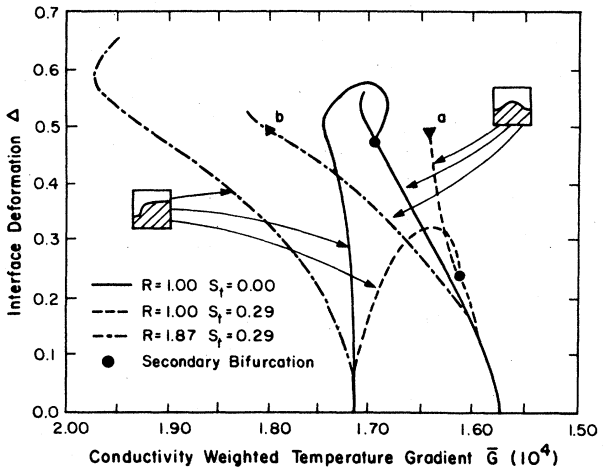

FIG. 2. Families of cellular interfaces represented by the interface deflection for $P=0.8$ and $\lambda=2.0$. Results for three different models are shown.

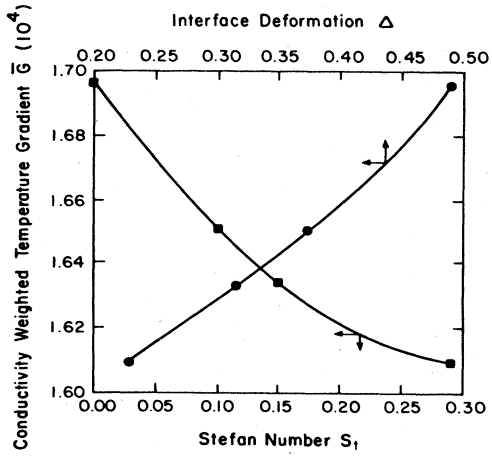

FIG. 4. Variation of temperature gradient and interface deflection for secondary bifurcation point as a function of Stefan number S_t for $P=0.8$ and $\lambda=2.0$.

percritically (with decreasing $\bar{G}$) before joining the second family at the secondary bifurcation point. Clearly, the structure of the solution families with and without latent heat were qualitatively similar.

The role of latent-heat release at the interface ($S_t \neq 0$) in establishing the relatively large quantitative differences in the evolution of the shape families can be understood by examining the isotherms in the melt and solid computed with $S_t=0.29$; samples of these are shown in Fig. 3(a). Even the small amount of latent heat released for this low growth rate caused the effective temperature gradient in the solid to be increased, as dictated by Eq. (3.3). When the melt-solid interface was curved the temperature distribution in the groove of the cell was set by the interaction of the temperature across the interface in a manner not given by the analysis for a nearly planar interface. Introducing latent heat with the conductivities of melt and solid equal ($R=1$) effectively increased the temperature gradient in the melt and decreased the deflection of the interface.

The first two families of cellular interfaces for the entire set of thermophysical parameters appropriate for Pb-Sb are also shown in Fig. 2; see the curves for $R=1.87$ and $S_t=0.29$. Both families evolve subcritically (to higher values of $\bar{G}$). For these parameter values no secondary bifurcation was calculated before the interface shapes in each family became nearly vertical along the wall of the groove. Calculations beyond the ends of the solution branches shown in Fig. 2 are useless because the Monge' representation of the shape $y=h(x)$ has failed. The secondary bifurcation most probably existed at a value of $\bar{G}$ greater than the critical value $\bar{G}_c^{(1)}$, and so the abrupt transition to cells with wavelength $\lambda/2$ would appear *before* the transition from the plane to cells.

The shifting of the solution branches to higher values of the weighted temperature gradient and to higher deflections for $R=1.87$ can be understood from the isotherms plotted as Fig. 3(b). With R greater than unity the gradient in the solid adjacent to the groove in the interface is less than in the melt; thus, increases in the composition in the groove must drive the interface deeper into the solid for the Gibbs-Thomson condition to be satisfied at the same imposed gradient in the melt.

The continuity of the secondary bifurcation point throughout the parameter space needed to span the solidification models in Table I is emphasized by calculating the variation of $\bar{G}_s^{(2)}$ with changes of several decades in the Stefan number.

The location of the secondary bifurcation point as a function of S_t for $R=1.0$ and $P=0.8$ is plotted in Fig. 4. As expected from the above discussion, increasing the

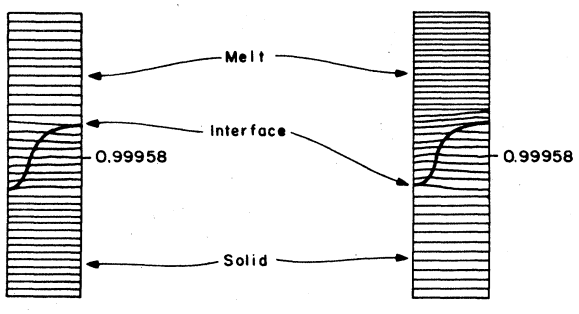

FIG. 3. Sample isotherms for calculations with (a) latent-heat release at the interface and (b) higher thermal conductivity in the melt than in the solid. These results correspond to the points marked *a* and *b* on Fig. 2. The spacing of the isotherms is $\Delta\theta=1\times10^{-5}$.

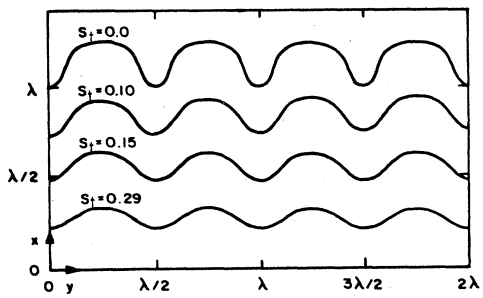

FIG. 5. Melt-solid interface shapes at secondary bifurcation points for four values of the Stefan number.

latent heat in the system stabilized the family of cells with $\lambda=2.0$ and decreased the value of $\overline{G}$ for the secondary bifurcation. The interface deflection at the secondary bifurcation point also decreased with increasing S_t, making the shapes more easily represented by the finite-element approximations; sample interface shapes corresponding to values of S_t and $\overline{G}$ at selected secondary bifurcation points are shown in Fig. 5.

B. High growth velocity

Increasing the growth velocity decreases the spatial wavelength of the most dangerous small-amplitude instability. Calculations are presented for $P=80$ for the spatial wavelength of $\lambda_c=0.09029$. Because we hold the reference length λ^* fixed, we rescale the deflections as $2\Delta/\lambda_c$, to be more representative of the actual deformation of the interface. The families of interfaces evolving from the first critical value of $\overline{G}$ are shown in Fig. 6 for $P=80$ and the parameter sets $(R=1,S_t=0)$, $(R=1.87,S_t=0.29)$, and $(R=1.87,S_t=1.2)$. No secondary bifurcation point was located for either set of calculations before the interface representation failed (the case for $R=1,S_t=0$ and $R=1.87,S_t=0.29$) or the melt became thermally undercooled (for $R=1.87$ and $S_t=1.2$), i.e., G became negative.

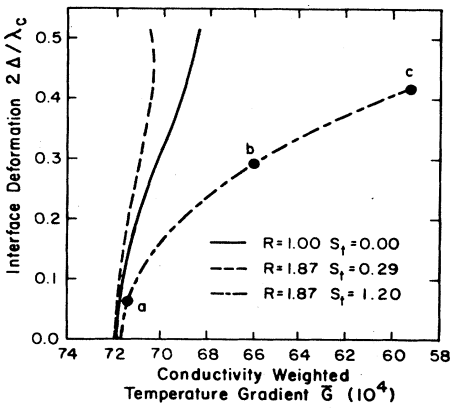

FIG. 6. Families of cellular interfaces represented by the interface deflection for $P=80$ and $\lambda=09029$. Results for three different models are shown. Points marked along the family for $S_b=1.2$ and $R=1$ denote positions of the isotherms and isoconcentration profiles shown in Fig. 7.

The calculations for $S_t=1.2$ for a range of $\overline{G}$ show the transition from a thermally superheated to an undercooled melt as the interface morphology varied. The isotherms and isoconcentration contours for three different values of $\overline{G}$ are plotted in Fig. 7; each solution (a)—(c) corresponds

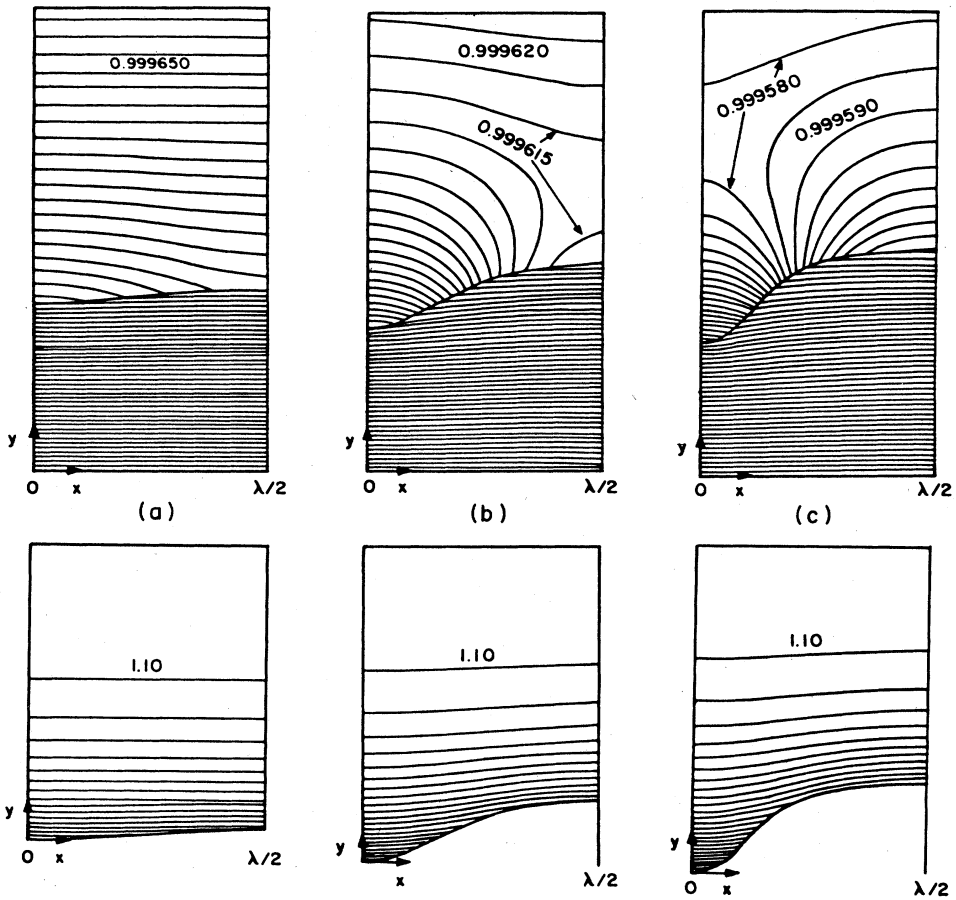

FIG. 7. Isotherms and isoconcentration contours for the parameter set $P=80$, $S_t=1.2$, and $R=1$. The values of the temperature gradient correspond to (a) 7.15×10^{-3}, (b) 6.61×10^{-3}, and (c) 5.91×10^{-3}. The spacings of the isotherms and isoconcentration curves are $\Delta\theta_m=5\times10^{-6}$, $\Delta\theta_s=1\times10^{-5}$, and $\Delta c=0.1$.

to a point on the curve in Fig. 6. For the highest value of $\overline{G}$, shown as Fig. 7(a), the isotherms in the melt are just deformed from those for a flat interface. Decreasing the temperature gradient into the melt caused latent heat to be released *into* the melt at the tip of the cell, instead of into the solid. Because the gradient was positive far into the melt, this extra amount of heat must be redirected through the melt back into the solid in the groove. This effect is demonstrated in Fig. 7(b) and is analogous to the results of McFadden and Coriell[7] for an Al-Ag system. Further decreasing the temperature gradient in the melt led to thermal undercooling away from the interface as shown by Fig. 7(c). Melt in the groove was not undercooled; heat released at the interface was conducted into the melt and passed through the groove into the solid. The concentration fields for all three cases show the formation of the diffusion boundary layer. The concentration field and interface shape deformed together, as expected from the linear analysis which sets the relevant length scale for the instability as D/V.

C. Effect of solid diffusivity

Introducing diffusion into the solid will smooth the concentration variations caused by the curvature of the interface and retard the deflection of the interface as the temperature gradient is decreased. To investigate the quantitative effects of $R_m > 0$, we performed calculations with the solutal model for R_m values of 0.05 and 1.0 and $P = 0.8$. The structures of the interface families determined for these two cases are shown in Fig. 8 and are identical to the results for $R_m = 0$ discussed above. The secondary bifurcation was located in each model for G less than 10% below the critical value for onset of the linear instability. Interface deflections were damped considerably by including solid diffusion; for $R_m = 1$, shapes in the family with $\lambda = \lambda_c$ never exceeded deflections of 0.4. Cells with nearly vertical sidewalls were computed for $R_m = 1$ and $\lambda = \lambda_c/2$, so that the Monge' representation again failed.

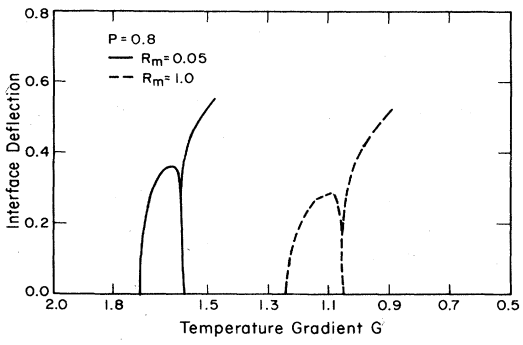

FIG. 8. Families of cellular interfaces for $P = 0.8$, $\lambda = 2.0$, and diffusivity ratios of $R_m = 0.05$ and 1.0 computed for the solutal solidification model.

V. CONCLUSIONS

This research and the results presented in UB clarify two major difficulties confronting either experimental or theoretical progress in the understanding of cellular pattern formation during solidification. First, the mathematical analysis of the evolution from planar to highly deformed interfaces is complicated by the secondary bifurcation demonstrated here, which halves the wavelength of spatially periodic cells. This transition is present in all the limits of the classical solidification model examined here, but may occur for interface shapes so deformed that they cannot be represented in the Monge' representation $y = h(x)$. Like the primary bifurcations from the planar state to cells of different, discrete wavelengths, the secondary junctions will only be destroyed by imperfections which break the basic symmetry in either the temperature field, concentration field, or the interface shape. The imperfection caused by a grain-boundary groove along the interface was analyzed in Ref. 10.

The location predicted for the secondary bifurcation and the shapes of the first two families of moderate-amplitude cells were very sensitive to the exact parameter values used in the calculation. Latent-heat release, the thermal conductivities in melt and solid, and the amount of solid diffusion all had large quantitative effects on the structure of the interfaces. Large amounts of solid diffusion made both families evolve supercritically (to lower values of G) and damped the amplitude of the cells. Increasing the growth rate had these same effects on the cells with $\lambda = \lambda_c$. Latent-heat release at the larger growth rates caused the temperature field to become locally, thermally undercooled at the cell tips, even when the temperature gradient far from the interface was positive.

These results all indicate the sensitivity of quantitative predictions for cellular morphologies to the assumptions made about the physics of the solidification process. Any attempt to match calculations with experiments near the onset of cellular growth will probably have to account for all these effects in the melt-solid system.

The second serious obstacle hindering further progress toward the theoretical calculation of deep cells is the tendency of the cell shapes with half the original wavelength to become vertical in the Monge' representation. If the deep cells observed experimentally are to be predicted to be a continuous evolution from the plane, they must appear along the second family of cell shapes or some family which bifurcates from it. We outline a method for continuing these calculations in the next paper in this sequence.[11]

ACKNOWLEDGMENTS

This research was supported by the Microgravity Sciences Program of the U.S. National Aeronautics and Space Administration, by the Mobil Foundation, by the Flat Plate Solar Array Project of the Jet Propulsion Laboratory, and by a grant from the Department of Energy for the use of the computer facilities at Los Alamos Scientific Laboratory.

*Present address: Department of Chemical Engineering, University of Pennsylvania, Philadelphia, PA 19104.

[1]W. W. Mullins and R. F. Sekerka, J. Appl. Phys. **35**, 444 (1964).
[2]D. Wollkind and L. Segel, Philos. Trans. R. Soc. London, Ser. A **268**, 351 (1970).
[3]M. Kerszberg, Phys. Rev. B **27**, 3909 (1983).
[4]G. Mathur and G. Dee, Phys. Rev. B **27**, 7673 (1983).
[5]J. S. Langer, Rev. Mod. Phys. **52**, 1 (1980).
[6]L. H. Ungar and R. A. Brown, Phys. Rev. B **29**, 1367 (1984).
[7]G. B. McFadden and S. R. Coriell, Physica (Utrecht) **12D**, 253 (1984).
[8]S. R. Coriell and R. F. Sekerka, J. Cryst. Growth **61**, 499 (1983).
[9]H. M. Ettouney and R. A. Brown, J. Comput. Phys. **49**, 118 (1983).
[10]L. H. Ungar and R. A. Brown, Phys. Rev. B **30**, 3993 (1984).
[11]L. H. Ungar and R. A. Brown, following paper, Phys. Rev. B **31**, 5931 (1985).